INTEGRATING LANDSAT-8, EMAG2V3, AND GGMPLUS GRAVITY DATA FOR GEOTHERMAL PROSPECT ZONATION AT DORMANT VOLCANO (CASE: MOUNT PUSUK BUHIT, NORTH SUMATRA, INDONESIA)

***Rina Dwi INDRIANA*[1], *Ihya Qothrunnada RAHMANI*[1]*, *Agus SETYAWAN*[1]*, *Ahmad Ali MUCKHAROM*[1] & *Richard LEWERISSA*[2]**

DOI: 10.21163/GT_2026.213.05

ABSTRACT

Indonesia has an estimated 23,591.75 MWe of geothermal potential, but exploration is costly and time-consuming. One of the islands in Indonesia, namely Sumatra, has 104 geothermal prospects, including the Simbolon–Samosir area, where Mount Pusuk Buhit has 150 MWe of inferred resources. This study uses satellite imaging to map surface and subsurface features at Mount Pusuk Buhit. Landsat-8 imagery is processed to create visualisations, while GGMPlus gravity data are analysed to map the land's structure. The NDVI calculation results are -0.51 to 0.87. The NDVI at the hot spring is lower than its surroundings, at -0.51 to 0.17. The research area has an LST of 19.72°C to 36.04°C. LST maps reveal localised heat anomalies on the flanks and foothills of Pusuk Buhit, some coinciding with known geothermal manifestations. Low NDVI values in these areas indicate reduced vegetation cover. Negative gravity anomalies are interpreted as fractured or fluid-influenced low-density zones, and positive anomalies indicate dense volcanic or intrusive bodies that may act as structural boundaries. Integrated LST and gravity overlay identifies four prospect zones. High LST coinciding with negative gravity is the most favourable for upflow. The Curie Depth Point values are generally around 28 to 31 km, which correlates well with heat flow values of around 48 to 50 mW/m². The results demonstrate the effectiveness and cost-effectiveness of combining Landsat-8 thermal, EMAG2V3, and GGMPlus gravity anomalies in assessing geothermal potential in volcanic terrains. The workflow can be used for other geothermal prospects in Indonesia.

Keywords: *Landsat-8, EMAG2V3, GGMPlus, geothermal, dormant, volcano, Pusuk Buhit.*

1. INTRODUCTION

Indonesia is located along a volcanic arc with abundant geothermal potential. Indonesia's estimated geothermal potential currently stands at 23,591.75 MWe, while its realised utilisation is only around 5%. In Sumatra, there are 104 geothermal prospects, including Mount Pusuk Buhit in Samosir Regency. The Simbolon–Samosir Geothermal Project working area, which is part of the Pusuk Buhit system, is estimated to have an indicated geothermal potential of approximately 150 MWe. Geothermal systems in volcanic regions are often difficult to map because of vegetation cover, weathering, and significant topographic variation. Mount Pusuk Buhit is a type-C volcano. Although no eruption has been recorded, the area is characterised by fumaroles and other signs of subsurface heat and fluid circulation. Such "dormant" systems are difficult to investigate because surface manifestations may be weak, while the subsurface structures that control permeability and fluid migration are hard to identify. Therefore, techniques capable of mapping both surface thermal manifestations and inferring subsurface structures would be highly useful.

[1]*Universitas Diponegoro, Department of Physics, Faculty of Science and Mathematics, 50275, Semarang, Indonesia; rinadwiindriana@lecturer.undip.ac.id (RDI), ihyaqothrunnada@alumni.undip.ac.id (IQR), agussetyawan@fisika.fsm.undip.ac.id (AS), alimuckharom@students.undip.ac.id (AAM).*

[2]*Universitas Papua, Department of Physics, Faculty of Mathematics and Natural Sciences, 98314, Manokwari, Papua Barat, Indonesia; r.lewerissa@unipa.ac.id (RL).*

[*]*Corresponding authors: ihyaqothrunnada@alumni.undip.ac.id, agussetyawan@fisika.fsm.undip.ac.id*

Geothermal exploration requires substantial resources, is time-consuming, and is often constrained operationally. Field mapping and sampling are hindered by steep topography, settlements, and weather conditions, all of which may increase uncertainty in geothermal identification. Satellite-based approaches can provide broad, efficient coverage, enabling geothermal target screening. Remote sensing has been used to highlight anomalous zones for further investigation in Indonesia and other volcanic regions (Bian et al., 2024; Weldeyohannes et al., 2022). Among the available satellite options, Landsat-8 OLI/TIRS has been widely used in preliminary geothermal studies through the analysis of surface thermal anomalies that may indicate the presence of geothermal resources (Azis et al., 2022). Various studies have demonstrated the effectiveness of Landsat-8 imagery for mapping land surface temperature in volcanic environments with geothermal resources (Saraswati et al., 2019).

In addition to thermal information, geological structural factors also play an important role in geothermal systems. Faults and fractures act as migration pathways for geothermal fluids from the reservoir to the surface (Grant & Bixley, 2011). In this study, we used Fault Fracture Density (FFD) analysis, which has been widely applied to delineate permeable zones (Ahmadi & Pekkan, 2021; Hutauruk et al., 2024). The integration of LST and FFD analyses is commonly treated as a unified interpretive framework and has been widely applied in geothermal exploration in various areas, both in active volcanic environments and non-volcanic geothermal systems (Alqahtani et al., 2023; Rabuffi et al., 2025; Rafiq et al., 2025).

To complement this geothermal potential analysis, we also used the gravity method based on the satellite-derived Global Gravity Model Plus (GGMPlus) dataset from Hirt et al., (2013). The gravity method can serve as a complementary tool for identifying subsurface structures, such as fractures, that act as pathways for ascending hot fluids. Gravity methods are widely used in geological investigations because they are sensitive to variations in rock density (Blakely, 1995; Telford et al., 1990). For example, gravity anomaly analysis has been proven to provide important information for detecting geothermal areas at Mount Ungaran and in other geothermal regions (Pratiwi et al., 2026; Setyawan et al., 2015, 2021, 2024). More recently, (Pratiwi et al., 2026) also successfully delineated structures controlling hydrothermal activity in the Arjuno–Welirang volcanic area. Therefore, the gravity method is highly suitable for the analysis conducted in this study.

Many regions worldwide (Indriana, 2019; Pramudya et al., 2025; Prihatini et al., 2025) have achieved successful results using this approach (Azis et al., 2022; Setyawan et al., 2015). However, validation data are still needed to assess whether the approach used in this study is effective. The next method we selected was the magnetic method, which is sensitive to the response of subsurface heat sources. We used Emag2v3 data from Meyer et al., (2017), which were analysed to estimate Curie depth. Several studies have also shown that Curie Point Depth (CPD) can be used to derive thermal gradients and heat flow based on the Curie temperature of magnetite (Demarco et al., 2021; Kassa et al., 2022; Kongpet & Kanjanapayont, 2024; Mono et al., 2018). A previous study by Muckharom et al., (2026) reported that the magnetic method is effective for estimating heat flow in several areas of Sumatra using Curie-depth analysis.

Based on these considerations, this study integrates several methods to assess geothermal potential in the Pusuk Buhit area, namely LST, FFD, gravity, and magnetic methods. The objective of this study is to identify geothermal potential in the Pusuk Buhit area in a more comprehensive manner. The originality of this study lies in the integrated use of geophysical and remote sensing methods. Its main novelty is the focus on the Pusuk Buhit area, which is still at an early exploration stage and therefore requires multiple types of data to support geothermal development. In addition, the novelty of this study lies in integrating geothermal and structural parameters, particularly through the application of the magnetic method to assess the regional-scale heat source, while hot fluids generally migrate through subsurface rock fractures or accumulate in reservoirs. The presence of these fractures and reservoirs is then identified using gravity and FFD methods, while surface thermal manifestations are analysed using the LST method. The study thus provides a more robust framework for reducing uncertainty in preliminary geothermal targeting, especially in dormant volcanic systems where surface manifestations are limited or ambiguous.

2. STUDY AREA

This study focuses on the Mount Pusuk Buhit geothermal zone, Samosir Regency (North Sumatra), which is part of the Simbolon Samosir Geothermal Working Area and is characterized by volcanic geomorphology with documented geothermal surface manifestations. Simbolon Samosir Geothermal area position 2°33'15.62" S - 2°38'34.39" S and 98°36'1,89 E - 98°41'22.65" E, the elevation height 904 - 2157 m (**Fig. 1**). Mt. Pusuk Buhit is classified as a dormant quaternary volcano. This research utilizes three satellite-compiled geophysical datasets: Landsat-8 OLI/TIRS, Global Gravity Model Plus (GGM+), and EMAG2-V3. Global Gravity Model Plus (GGMPlus) imagery to derive surface indicators (composite bands, NDVI, and land surface temperature). GGMPlus satellite gravity data to analyze subsurface density structure patterns at approximately ~200 m spatial resolution. EMAG2-V3 compiled magnetic anomaly data to estimate Curie Point Depth (CPD) and derive thermal proxies (geothermal gradient and heat flow) at a regional scale (Hirt et al., 2013; Meyer et al., 2017). Landsat-8 OLI/TIRS is downloaded from USGS, GGMPlus is free support from Curtin University, and EMAG2-V3 is free from ICGEM.

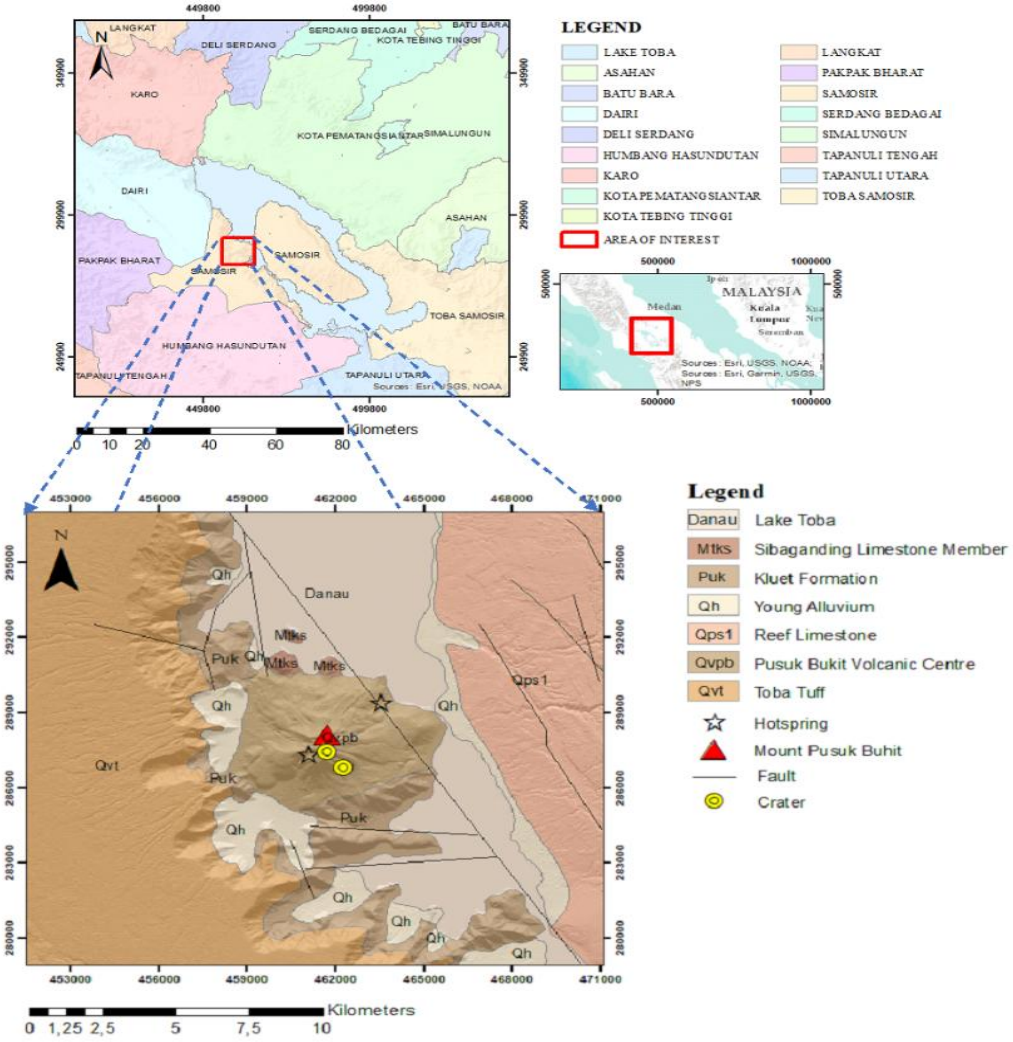

Fig. 1. The research area and geological map of Pusuk Buhit.

Based on the geological map on **Fig. 1**, The Sidikalang and (part of) Sinabang, Sumatra by Aldiss, (1983), the formations in the study area consist of the Toba Tuff Formation (Qvt) with rhyodacite tuff (partially cemented), the Pusuk Buhit Formation (Qvpb) with dacite and/or rhyolite rock types, the Kluet Formation (Puk) with metacuarzic sandstone, metaclastic, shale, and phyllite rock types, the Kualu Formation (Mtks) with sibaganding limestone: biocalcilutite, and the Alluvium Formation (Qh) with gravel, sand, mud, fan conglomerate, diatomaceous earth, and coral.

3. DATA AND METHODS

3.1. Landsat-8 preprocessing and surface parameter retrieval

3.1.1. Normalized Difference Vegetation Index (NDVI)

Vegetation cover was quantified using the Normalized Difference Vegetation Index (NDVI) to reduce land-cover bias in thermal interpretation and to support emissivity estimation in heterogeneous volcanic terrain. NDVI was calculated as equation (1).

$$\mathrm{NDVI} = \frac{\mathrm{NIR} - \mathrm{Red}}{\mathrm{NIR} + \mathrm{Red}} \tag{1}$$

In this respect, NIR and Red represent near-infrared reflectance and red reflectance, respectively. Typically, low NDVI values are associated with sparse vegetation, exposed soil, or altered surface materials, whereas higher NDVI values are associated with more vegetative surfaces (Alqahtani et al., 2023).

3.1.2. Thermal radiance and brightness temperatures (TIRS)

Thermal processing used Landsat-8 TIRS measurements, beginning with conversion from the thermal band digital number (DN) to spectral radiance was expressed as equation (2).

$$L_\lambda = M_L \cdot Q_{cal} + A_L \tag{2}$$

where L_λ is spectral radiance, M_L is the radiance multiplicative scaling factor, A_L is the radiance additive scaling factor, and Q_{cal} is the quantized calibrated pixel value (DN).

Brightness temperature was then computed as equation (3).

$$T_B = \frac{K_2}{\ln\left(\frac{K_1}{L_\lambda} + 1\right)} \tag{3}$$

where T_B is the at-sensor brightness temperature (K) and K_1, K_2 are band-specific thermal calibration constants.

This radiance-to-temperature step provides a physically consistent thermal measure before correcting for surface emissivity.

3.1.3. Land Surface Temperature (LST) and emissivity correction

Land Surface Temperature (LST) was derived from brightness temperature with emissivity correction to better represent true surface conditions. A commonly used form that is adapted to the emissivity shown in equation (4).

$$\mathrm{LST} = \frac{T_B}{1 + \left(\frac{\lambda T_B}{\rho}\right) \ln(\varepsilon)} \tag{4}$$

where λ is the effective thermal wavelength, $\rho \approx 1.438 \times 10^{-2}$ m · K(with $\rho = h\,c/\sigma$), and $\varepsilon$is land surface emissivity.

Emissivity was estimated via an NDVI-based approach to account for mixed land-cover conditions. Vegetation proportion (PV) was calculated as equation (5).

$$PV = \left(\frac{\mathrm{NDVI} - \mathrm{NDVI}_{min}}{\mathrm{NDVI}_{max} - \mathrm{NDVI}_{min}}\right)^2 \tag{5}$$

and emissivity was approximated using equation (6).

$$\varepsilon = 0.004 \cdot PV + 0.986 \tag{6}$$

This NDVI-based emissivity estimation is widely used to reduce LST error associated with variable surface materials (soil, vegetation, water) and is particularly relevant in volcanic terrains where alteration and land cover vary over short distances (Alqahtani et al., 2023).

3.2. GGMPlus gravity processing

The gravity field data used for this research is provided by GGMplus, a high-resolution representation of the global gravity field with nominally 200 m resolution on land. GGMplus is based on satellite gravimetry observations (GRACE and GOCE), terrestrial gravimetry observations, airborne gravimetry, marine gravity observations from altimetry, and models of topographic mass (Hirt et al., 2013). These gravity disturbances are ideal for geological or geophysical studies at a regional and local level, particularly over areas with limited land-based gravimetry data. Gravity data are affected by the simultaneous action of latitude, topography, the Earth's rotation rate, and the subsurface mass distribution.

The geological information on subsurface density changes can be uncovered after a series of standard corrections for gravity are applied to the data. The free-air correction is due to the decrease in gravity from the topographical datum to the observation level, where there is no mass between the observation level and the topographical datum on the ground.

The Bouguer and Terrain correction affected of the attraction due to the mass between the observation level and the datum by simulating an infinitely extended horizontal bed of homogeneous rocks of 2.67 g/cm³ density for continental regions (Blakely, 1995). The Bouguer anomaly was calculated using equation (7).

$$\Delta g_{Bouguer} = g_{obs} - g_n + \delta gFA - \delta gB + \delta gT \tag{7}$$

where g_{obs} is the observed gravity, g_n is the normal gravity, δgFA is the free-air correction, δgB is the Bouguer correction, and δgT is the terrain correction.

The terrain correction is particularly important in regions with significant topographic relief and improves the accuracy of the Bouguer anomaly (Arifianto et al., 2025). Analysis of subsurface density variations using local anomaly data. Separation of local and regional anomalies using the upward continuation method. Further study to strengthen the vertical and horizontal subsurface identification rock density variation model created using a 2D inversion model.

3.2.1. Inverse model

Gravity Inversion modelling is a quantitative geophysical method aiming to recover the subsurface pattern of density contrast responsible for a set of observed gravity anomalies, formulated as a solution of a regularised inverse problem. The inversion formula was calculated using equation (8).

$$\mathbf{d}=\mathbf{G}\mathbf{m} \tag{8}$$

where $\mathbf{d}$ is the vector of observed gravity anomalies at measurement locations, $\mathbf{m}$ is the model parameter vector (density contrasts in discretized cells), and $\mathbf{G}$ is the sensitivity matrix that relates the influence of each model cell on each observation.

The entries of $\mathbf{G}$ are computed from Newton's law of gravitation for the chosen cell geometry (e.g., prisms, tetrahedra). Inversion solves for $\mathbf{m}$ by minimizing an objective function and is calculated using equation (9).

$$\phi(\mathbf{m})=\|\mathbf{W}_d(\mathbf{d}_{obs}-\mathbf{G}_m)\|^2+\lambda^2\|\mathbf{W}_m(\mathbf{m}-\mathbf{m}_{ref})\|^2 \tag{9}$$

where $\mathbf{d}_{\mathrm{obs}}$ are observed data, $\mathbf{W}_d$ is the data weighting matrix accounting for measurement uncertainties, $\mathbf{W}_m$ is a regularization operator enforcing smoothness or focusing constraints, $\mathbf{m}_{\mathrm{ref}}$ is a reference model, and λ is the regularization parameter balancing data misfit and model complexity (Blakely, 1995; Y. Li & Oldenburg, 1996).

3.3. Curie Point Depth (CPD)

Regional magnetic anomaly data were obtained from the EMAG2-V3 global compilation (2 arc-min grid at ~ 4 km altitude), which integrates satellite, marine, airborne, and shipborne magnetic surveys and applies kriging-based interpolation to improve consistency across heterogeneous survey tracks (Meyer et al., 2017). In CPD analysis, the grid was projected into overlapping sub-areas to support local spectral estimation. The CPD was estimated using the 2D spectral method applied to each windowed magnetic anomaly subset. The radially averaged power spectrum was computed from the 2D Fourier transform, and linear segments of ln[P(k)] versus wavenumber k were fitted to estimate depths of the magnetized layer following established formulations (C. F. Li et al., 2017). Z is the depth (vertical distance) from the Earth's surface to a magnetic source, measured positive downward, typically expressed in kilometers (km). The depth to the top of the magnetic source (Zt) was estimated from the high-wavenumber slope (s_(high)) and the centroid (Z_o) from the low-wavenumber slope (s_(low)) using the following relationship. That calculated using equation (10).

$$\ln P(k) = lnC - 2kZ \tag{10}$$

The depth to the bottom of the magnetized layer (Zb), interpreted as CPD, was then obtained using the relation proposed in the centroid method (Okubo & Matsunaga, 1994).

$$\mathrm{Z}_b = 2\mathrm{Z}_0 - \mathrm{Z}_\mathrm{t} \tag{11}$$

3.3.1. Geothermal gradient and heat flow from CPD

Assuming the Curie temperature (Tc) of dominant magnetic minerals is ~580°C, the geothermal gradient (G) can be approximated from the Curie isotherm depth as equation (12).

$$\frac{dT}{dZ} = \frac{\theta}{Z} = \frac{580℃}{Z_b} \tag{12}$$

where T is the mean surface temperature (or a reference near-surface temperature), and Z_b is CPD (Kongpet & Kanjanapayont, 2024; Maden et al., 2009).

Geothermal heat flow (Q) was then estimated using Fourier's law in equation (13).

$$Q = \lambda \frac{dT}{dZ} = \lambda \left(\frac{580°C}{Z_b}\right) \tag{13}$$

where λ is the thermal conductivity of the crustal column (Saada, 2016). Spatial patterns of CPD, geothermal gradient, and heat flow were mapped and later integrated with the surface thermal and gravity-derived structural indicators.

The complete research flowchart is presented in **Fig. 2**.

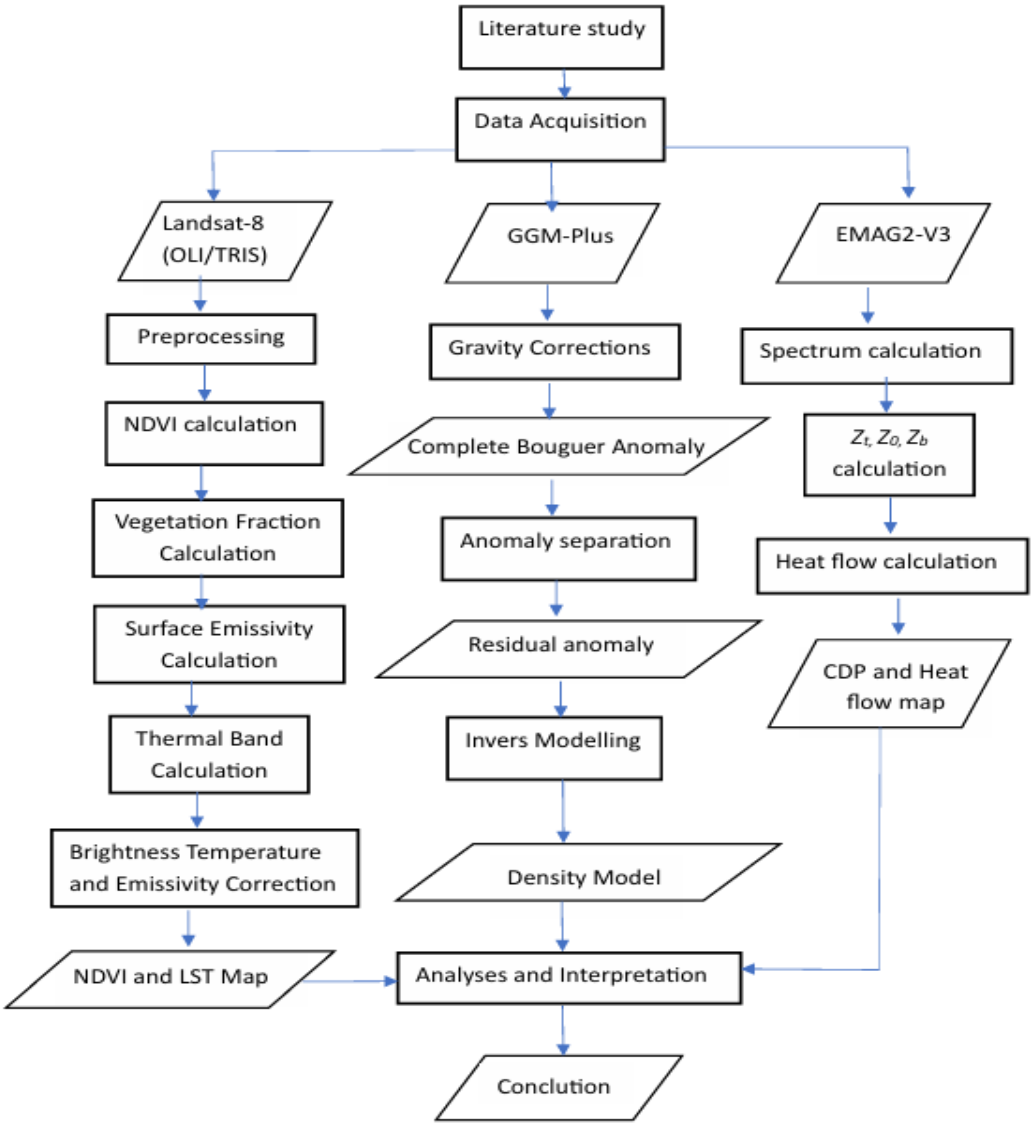

Fig. 2. The research flowchart.

4. RESULTS

4.1. NDVI and LST

The Landsat 8 composite band provides a first glance at heterogeneity, where it is possible to distinguish geomorphological differences based on volcanic cones, flow units, and potential alteration areas at Mount Pusuk Buhit. The geomorphological differences are important as geothermal surface features in volcanic environments are known to be concentrated around areas that are characterised by alterations, exposed ground, and unique geomorphological features that indicate permeability. In this study, the composite imagery is used to contextualise the spatial distribution of subsequent thermal indicators by delineating surface units where thermal behaviour is expected to differ due to material properties and land cover. NDVI mapping shows in **Fig. 3a**, a clear spatial variation in vegetation density across the Pusuk Buhit.

The NDVI calculation results are -0.51 to 0.87. The NDVI at the hot spring is lower than its surroundings, at -0.51 to 0.17. The northeastern hot spring has a high anomaly pattern flanking the fault line. Other areas with low NDVI include Lake Toba and residential areas. Mount Pusuk Buhit has relatively well-maintained vegetation density. NDVI assists in the identification of areas that are sparsely vegetated but could be geothermally significant because the heat anomaly is easier to detect where the surface energy contrast caused by vegetation is low. Areas that have high NDVI values suggest that the vegetation is dense and could potentially obscure the surface heat through the processes of evapotranspiration and shading. In view of the above, the heat anomaly needs to be assessed in the context of vegetation. As already stated, the NDVI-heat anomaly is consistent with other research that suggests that vegetation indices show positive associations with geothermal-related heat anomalies where surface heat is high in areas that have less vegetation (Alqahtani et al., 2023; Azis et al., 2022; Chan & Chan, 2023).

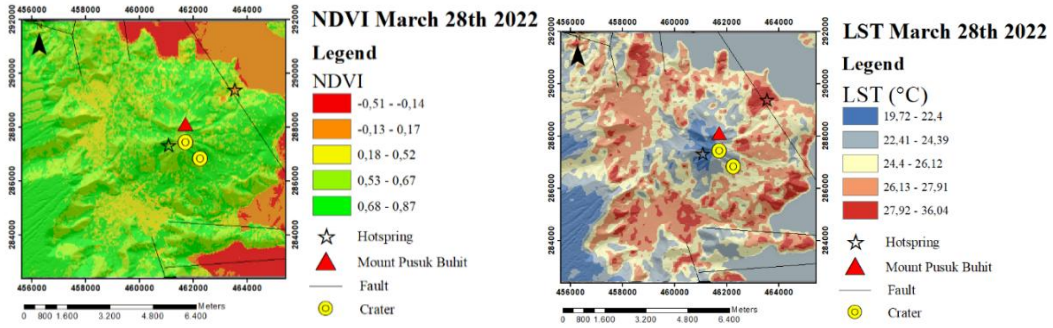

a. b.

Fig. 3. Spatial distribution derived from Landsat-8 TIRS across the study area a) NDVI values highlighting areas of low vegetation density associated with altered or thermally affected zones, b) Land Surface Temperature (LST) showing the distribution of surface thermal anomalies

The entire research area has an LST of 19.720°C to 36.04°C. The peak area of Mount Pusuk Buhit has a low LST compared to its surroundings. There are 2 hot springs, on the west side of the crater and on the northeast of the crater. Hot spring in the northeast are in a fault area that trends southeast - northwest. The LST values at hot springs are different, ranging from 22.41°C to 24.39°C. Emissivity-corrected LST mapping reveals that localized thermal anomalies are largely confined along the flanks of Mount Pusuk Buhit (**Fig. 3b**). The hotspots are not continuous but rather localized, implying focused permeability pathways for near-surface geothermal activity. LST anomalies indicate increased flow of heat in the vicinity of near-surface fluids moving upward or heat flow from underlying hotter regions. This finding is consistent with research that associates Landsat thermal

anomalies with geothermal phenomena, such as hot springs and fumaroles. In previous research carried out in Taiwan and Indonesia, it has been known that satellite thermal anomalies tend to coincide with geothermal activity, thereby making Landsat a thermal anomaly mapping tool employed for the investigation of geothermal potential (Chan & Chan, 2023; Muhajir et al., 2023). In Pusuk Buhit, Landsat-8 thermal anomaly regions are identified as potential domains of geothermal manifestation to be verified by additional subsurface factors.

4.2. CBA and Residual Anomaly

The GGMplus data used is the gravity disturbance, which is then corrected to CBA. Bouguer and Terrain corrections use an average density of 2.67 g/cc. CBA is obtained in the range of -86.6 mGal to -74.5 mGal. High anomalies (-81 mGal to 74.5 mGal) cover Mount Pusuk Buhit, while low anomalies (-86.6 mGal to 83 mGal) are in the Pusuk Buhit peak area. The distribution of CBA values is mapped as shown in **Fig. 4a**. In the processed GGMPlus gravity anomaly map, there are identifiable regions with positive and negative values. The negative regions point to regions of lower density, which may include regions with fractures or hydrothermal zones associated with geothermal resources. The positive regions may point to regions with higher density associated with competent volcanic rocks.

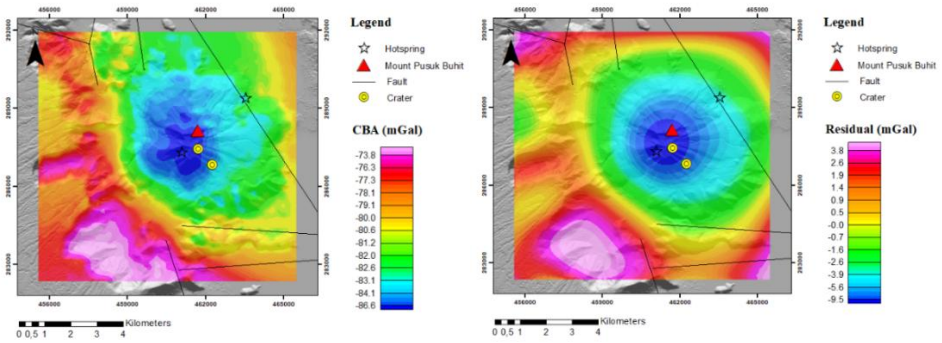

a. b.

Fig. 4. a) Bouguer gravity anomaly map and b) residual anomaly map beneath Mount Pusuk Buhit derived from GGMPlus

Further analysis was conducted to separate local and regional anomalies using the upward continuation method. Upward continuation is an effective approach to minimize high-frequency noise and focus interpretation on regional gravity trends relevant to geothermal systems (Muhajir et al., 2023). By obtaining regional values, local/residual anomaly values can be obtained.

Fig. 4b shows a map of the distribution of residual anomaly values ranging from -9.5 mGal to 3.8 mGal. The geothermal area is situated in a low to moderate anomaly zone, characterized by blue to green colors (-9.5 mGal to -2.6 mGal). This matches the conventional structural interpretation of geothermal data, where positive values are associated with magmatic intrusions and/or structural highs, and negative values are associated with fractured and altered areas where geothermal fluids might be present (Alqahtani et al., 2023). In this context, the gravity map of the Pusuk Buhit area serves as an indicator of the underlying structural characteristics, assisting in determining whether the thermal anomalies are of geothermal origin or of a transient nature.

4.3. Density Modeling

Subsurface modeling of the Pusuk Buhit area based on residual anomaly data, as shown in **Fig. 5.** Inverse modeling was performed on the B-B' traverse with an SN direction crossing the central formation of Pusuk Buhit (Qvpb), the Kluet formation (Puk), faults, and hot spring manifestations.

The rock density beneath the B-B' line ranges from 1.97 g/cc to 2.96 g/cc. The geothermal area has a density of 2.3 g/cc to 2.65 g/cc and is associated with a low-density zone in the south. There is a medium to low-density zone to the south, the position of which coincides with the previously mapped geological structure (fault).

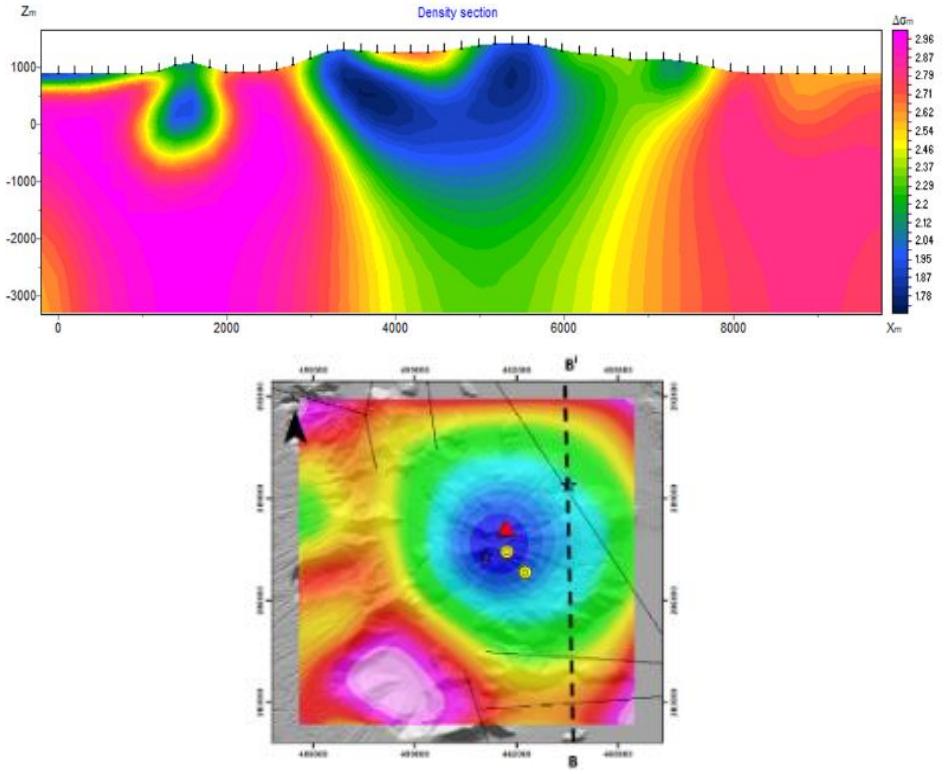

Fig. 5. Subsurface density model Pusuk Buhit area (line 463261,592 m E).

4.4. Fault and Fracture Density (FFD) Analysis

A map showing the spatial distribution of fracture linear density values is presented in **Fig. 6**.

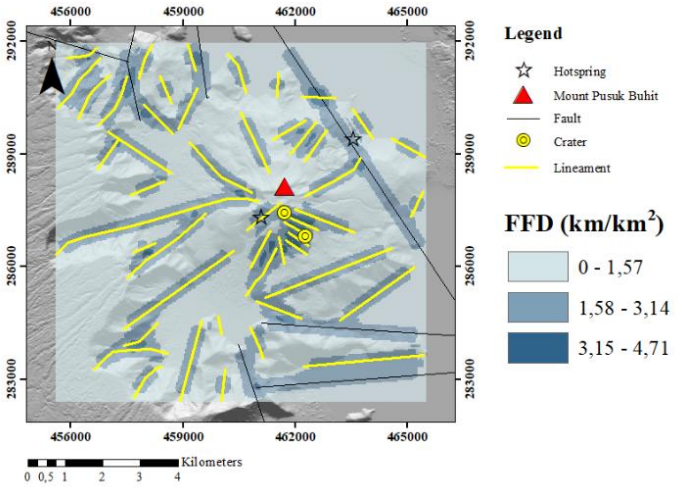

Fig. 6. Fracture Density (FFD) Pusuk Buhit.

High density values, ranging from 3.15 to 4.71 / km, are evident along the mountain peaks, while low to medium density values range from 0 to 1.57 /km and from 1.58 to 4.14 /km, respectively. Hot water manifestations pass through faults in areas with medium fracture density. High-density values are found on Mount Pusuk Buhit, which is related to the deformation of the volcano/past volcanic activity of Mount Pusuk Buhit, resulting in the formation of many faults and fractures.

Mount Pusuk Buhit is a recharge area in the geothermal system, serving as an entry point for rainwater to fill the permeable zone in the geothermal system. The lack of hot springs in the summit area and the presence of the hot springs on the northeastern slope of the mountain can be explained on the basis of geological structure. The area of manifestation of the hot spring, as indicated in the map, is located in the junction zone of the fracture system and the fault. This suggests that the structure is likely the path of hydrothermal fluid rising from below the surface. Additionally, this reinforces the assumption that Mount Pusuk Buhit still exhibits geothermal activity, even though it is currently inactive.

4.5. Curie Point Depth (CPD) and Heat Flow (HF)

Fig. 7, the trend of Curie Depth Point (CPD) data to surface heat flow values at the Pusuk Buhit geothermal area shows a distinct inverse trend, where areas with shallower Curie depths relate to areas of relatively high surface heat flow. The Curie Depth Point values are generally around 28 to 31 km, which correlates well with heat flow values of around 48 to 50 mW/m², which show a moderate heat flow regime. This trend correlates well with the theory of conductive heat flow, where the heat flow values increase as the Curie depth values decrease.

In the absence of very shallow Curie depths (<15 km), as would be expected in an actively magmatic geothermal environment, a moderately low heat flow as determined from the CPD data suggests a deep thermal source and not a magma chamber. This suggests that Mount Pusuk Buhit is a dormant (Type-C) volcanic environment in which there is little manifestation at the surface and which is controlled more by regional processes than magmatic intrusions.

The relationship between Curie Depth Point (CPD) and heat flow observed in this study is consistent with recent spectral analyses applied to aeromagnetic data, which demonstrate that shallower Curie depths correspond to higher geothermal gradients and increased surface heat flow (Ejiga et al., 2022). Specifically, several regional studies have shown that mapping CPD provides an indirect but reliable approach for estimating the thermal regime of the crust, including geothermal gradient and heat flow distribution (Boumehdi et al., 2025; Muckharom et al., 2026). The determined CPD and heat flow values provide a basis for understanding the thermal structure of crustal segments and support the interpretation of subsurface heat transfer processes in geothermal contexts.

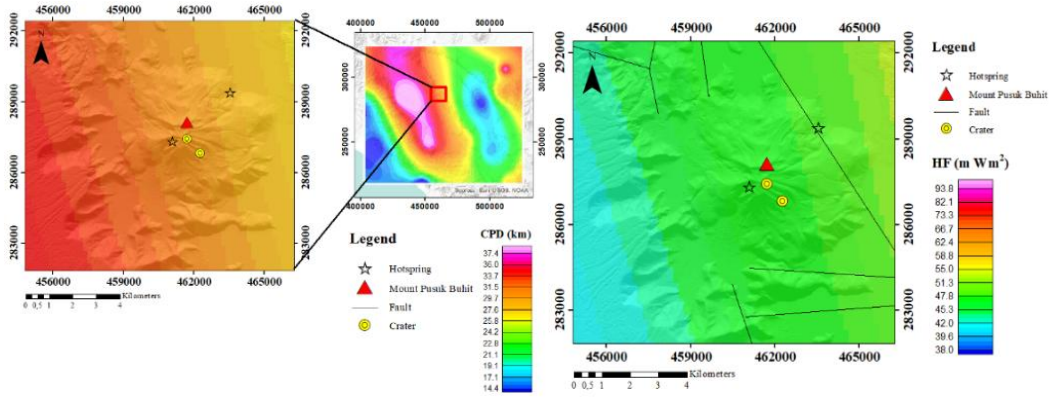

Fig. 7. Integrated interpretation of surface and subsurface results

Integration analysis was performed by overlaying LST, NDVI, CPD, CBA, residual gravity anomaly, and subsurface density model profiles on the line 463261.592 m East. This line passes through two fault zones (east-southwest and east-northwest faults) and geothermal manifestations. The analysis presented in **Fig. 8** shows a consistent spatial association between surface heat signals, subsurface heat signals, and subsurface density structures. The north-south cross-section in the figure demonstrates the integrated response of surface thermal anomalies, gravity anomalies, subsurface density patterns, and estimates of Curie Point Depth (CPD)-Heat Flow (HF), which distinguish two major sections: the crater area (grid points 23-30) and the manifestation area (grid points 35-42).

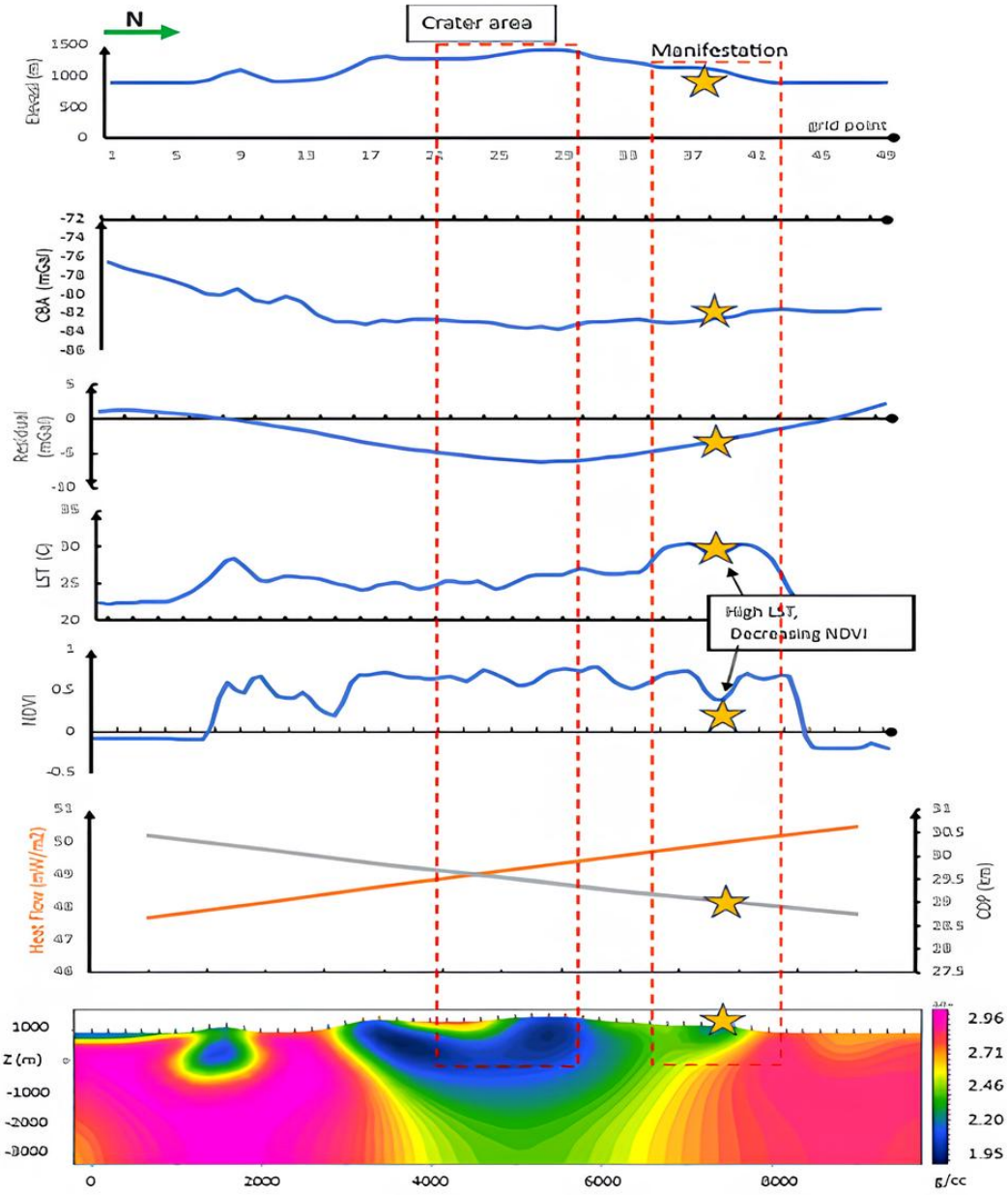

Fig. 8. Integrated map overlaying LST anomalies and gravity anomaly patterns to delineate prospective geothermal zones at Mount Pusuk Buhit.

In terms of morphological characteristics, the crater area is found within the area of relatively higher topography, while the manifestations are found downslope following the major topographic ridge, suggesting that the surface expressions of geothermal activity are not controlled by topography alone but are dominated by subsurface patterns and structural pathways that channel heat and fluid migration. The Complete Bouguer Anomaly (CBA) is characterized by a regional decrease from the northern part of the area toward the central part of the section, followed by a trend of flattening. Significantly, there is a slight modification of the trend of the CBA near the manifestation area, which suggests a change of the regional density domain, perhaps from lower-density volcanic-altered rocks to a more competent and higher-density block, or the influence of a major structural boundary. This is also reflected by the residual gravity anomaly, which is more responsive to shallow-to-intermediate crustal density contrasts, as the residuals progressively become more negative toward the central part and then reverse, becoming progressively more positive (less negative, approaching zero) at the manifestation area. This is generally expected for a local density contrast or a sharp lateral density transition across a lithologic contact or fault boundary. In geothermal areas, this kind of residual gravity anomaly is generally interpreted as a structurally damaged and fractured area of higher permeability, which acts as a structurally controlled conduit for the upward migration of hydrothermal fluids and heat.

The strongest surface thermal anomaly is captured in the Land Surface Temperature (LST) curve, which shows a clear, localized LST maxima in the manifestation area (around 300°C - 32°C). The sharpness of the LST maxima and the fact that it does not correlate straightforwardly with topography argue for a localized, geothermal heat leakage feature, rather than a strictly atmospheric and topographic feature. Most importantly, the LST maxima are associated with a simultaneous decrease in NDVI for the same area, such that the high LST and decreasing NDVI feature together offer a reliable proxy for the presence of non-atmospheric, high-temperature conditions, indicative of stressed and possibly altered biologic and surface conditions in response to the presence of subsurface heat and hydrothermal fluids.

At depth, the density cross-sectional profile further emphasizes the structural control, in which the crater area is positioned over a relatively large, lower-density area possibly indicative of unconsolidated volcanic materials, pervasive alteration, and a possibly fractured and porous area, and in which the manifestation area shows a sharp density gradient, from lower to higher density, indicative of a block boundary and large fault/contact, which may act to channel fluids upwards. This suggests that surface manifestations are preferentially found not necessarily over the center of the density-low area, but over its edge, where the density and structural contrasts are largest, and where permeability contrasts may act to channel and concentrate the release of hydrothermal fluids.

These multiparameter measurements are mutually consistent within the CPD-HF panel, which indicates an inverse correlation between Curie depth and heat flow. The data point corresponding to the manifestation zone is distinguished by its relatively shallower CPD (29 km) and its higher HF (48-50 mW/m^2) value than the other profiles on the transect, which suggests an elevated upper-to-middle-crustal thermal regime and an increased geothermal gradient below the manifestation zone. While the CPD measurements are generally in the moderate to deep range and do not suggest an abnormally shallow Curie depth as would be expected for shallow, magmatically active geothermal systems (CPD < 15 km), the spatial coincidence of the elevated HF, the LST peak, the low NDVI, the residual gravity transition, and the sharp density boundary strongly suggests the presence of a deep-seated regional heat source underlying the Pusuk Buhit system as a dormant volcanic geothermal system, and the surface expression is due to the structurally focused flow of heat and fluid. In this model, the crater area is dominantly a morphologic and/or alteration-recharge area, while the manifestation zone is the discharge area, which develops where the structural permeability is maximal, as indicated by the gravity and density contrasts, and is the location where the subsurface thermal anomaly is optimally manifested on the surface through the LST and the corresponding NDVI reduction. These integration findings are consistent with previous studies that validate the combined approach of thermal remote sensing and gravity to delineate geothermal prospect zones.

In various prospects, including case studies in Indonesia, thermal anomalies from Landsat/ASTER are reported to correlate with gravity anomalies indicating subsurface reservoirs, thereby increasing confidence in integrated surface and subsurface screening (Muhajir et al., 2023; Weldeyohannes et al., 2022). The comprehensive analysis is characterized by surface indicators (LST anomalies, reduced vegetation through NDVI, shallow CPD compared to the surrounding area, alignment and position of manifestations) supported by subsurface structural evidence (gravity-based density contrasts and indications of fracture domains). This approach is consistent with commonly used criteria for defining more reliable geothermal prospect zones (Bian et al., 2024; Chen et al., 2021).

5. DISCUSSIONS

Compared with geothermal systems in similar volcanic environments, such as Taiwan and the Ethiopian Rift (Chan & Chan, 2023; Weldeyohannes et al., 2022), the Pusuk Buhit system exhibits a comparable pattern. Surface thermal anomalies are spatially associated with structure-controlled permeability zones, rather than directly overlying the primary heat source. In contrast to active volcanic systems, which typically have a shallow Curie Point Depth (CPD) (<15 km), the deeper CPD values in the Pusuk Buhit area (28–31 km) suggest that the geothermal system is controlled more by regional conductive heat flow than by shallow magmatic intrusions, which are characteristic of dormant volcanic systems.

Gravity data strengthen the geological validation of the surface thermal model. Negative gravity anomalies may indicate low-density zones associated with fractures, hydrothermal alteration, and/or fluids. In contrast, positive anomalies reflect high-density rocks, such as intrusive or compacted volcanic rocks that could act as heat sources or fluid barriers. These patterns are also observed in other volcanic environments, where positive anomalies are linked to heat sources and negative anomalies to fracture zones or hydrothermal systems (Alqahtani et al., 2023; Pratiwi et al., 2026).

Furthermore, the presence of LST anomalies above the gravity structure strengthens the evidence that the geothermal system at Mount Pusuk Buhit is controlled by geological structures. Areas with high LST values indicate heat flow to the surface through fractures and faults, which can also be identified through structural patterns derived from gravity anomalies and remote sensing (Muhajir et al., 2023; Rabuffi et al., 2025). The integration of Landsat-8 thermal imagery and the gravity satellite GGMPlus has been shown to improve exploration capabilities by linking surface temperature variations with subsurface structural patterns associated with geothermal systems (Muhajir et al., 2023; Weldeyohannes et al., 2022).

The Landsat-8 and GGMPlus integration approach provides key advantages for early-stage exploration. It lowers costs, reduces risks, and efficiently covers large areas (Bian et al., 2024; Muhajir et al., 2023). The best target zones are where LST anomalies—unusual surface heat—align with gravity-derived structures that indicate subsurface density changes. These areas meet two main geothermal criteria: available heat and pathways for fluid flow, such as faults or fractures. This integration approach identifies these features by combining surface thermal indicators with subsurface density variations (Putri et al., 2021).

In this context, the Curie Point Depth (CPD) derived from magnetic data reveals regional variations in thermal conductivity. However, it does not directly map local upflow zones controlled by fault permeability. Therefore, the difference between the surface hotspot and the shallowest CPD does not necessarily lower geothermal prospectivity. Instead, it shows that the geothermal system at Mount Pusuk Buhit is interpreted as structure-controlled, with local effects on regional thermal trends. Also, interpreting the link between surface features and CPD needs caution, since the EMAG2-V3 model shows different scales that better reflect regional features. The CPD is best for outlining a regional thermal framework. For prospect mapping, higher-resolution data (such as structural mapping, geochemistry, resistivity (e.g., MT), and multi-temporal LST–NDVI analysis) are needed.

6. CONCLUSIONS

This study confirms that the integration of Landsat 8 surface thermal anomalies with GGMPlus gravity data provides a reliable and cost-effective approach for preliminary geothermal exploration at Mount Pusuk Buhit. The NDVI calculation results are -0.51 to 0.87. The NDVI at the hot spring is lower than its surroundings, at -0.51 to 0.17. The research area has an LST of 19.72°C to 36.04°C. The spatial coincidence of high LST anomalies with negative gravity values indicates that geothermal heat and fluids are preferentially channeled through low-density subsurface zones associated with fractures, altered rocks, and fault-controlled permeability, while positive gravity anomalies reflect denser volcanic or intrusive bodies that may act as heat sources or structural barriers. The strong correspondence between LST anomalies and gravity-defined structural corridors supports a structurally controlled geothermal system rather than a shallow magmatic heat source, with low NDVI–high LST areas further suggesting surface thermal stress or hydrothermal alteration. The Curie Depth Point values are generally around 28 to 31 km, which correlates well with heat flow values of around 48 to 50 mW/m². Although Curie Point Depth (CPD) derived from magnetic data effectively constrains the regional thermal regime, it does not resolve localized hydrothermal upflow, indicating that the lack of coincidence between surface hotspots and shallow CPD does not preclude geothermal prospectivity.

This study shows that integrating Landsat 8 thermal data with GGMPlus gravity data provides an effective and low-cost framework for preliminary geothermal exploration at Mount Pusuk Buhit. Its main scientific contribution lies in demonstrating that geothermal surface manifestations are spatially associated with gravity-defined low-density structural zones, highlighting the dominant role of fault- and fracture-controlled permeability in the geothermal system. In addition, the study clarifies that Curie Point Depth reflects the regional thermal structure rather than localized hydrothermal upflow. These findings support the use of integrated thermal and gravity analysis as a transferable prefeasibility tool for geothermal exploration in complex volcanic settings.

ACKNOWLEDGEMENT

We acknowledge the use of Landsat data provided by the United States Geological Survey (USGS), GGMPlus gravity data were freely provided by Curtin University, the EMAG2-V3 magnetic model was obtained free of charge from the International Centre for Global Earth Models (ICGEM). The authors acknowledge the use of AI-based tools for assistance with language polishing and manuscript organization. The tools did not influence the scientific content, and all responsibility for the manuscript rests with the authors.

REFERENCES

Ahmadi, H., & Pekkan, E. (2021). Fault-based geological lineaments extraction using remote sensing and gis—a review. *Geosciences (Switzerland)*, *11*(5). https://doi.org/10.3390/geosciences11050183

Aldiss, D. T. (1983). *Geologic map of the Sidikalang quadrangle, Sumatra 1:250,000*.

Alqahtani, F., Aboud, E., Ehsan, M., Naseer, Z., Abdulfarraj, M., Abdelwahed, M. F., & El-Masry, N. (2023). Geothermal Exploration Using Remote Sensing, Surface Temperature, and Geophysical Data in Lunayyir Volcanic Field, Saudi Arabia. *Sustainability (Switzerland)*, *15*(9). https://doi.org/10.3390/su15097645

Arifianto, I., Nishijima, J., & Wibowo, R. C. (2025). Maetec: An Optimized Matlab-Based Approach For Accurate And Efficient Terrain Correction In Complete Bouguer Anomaly. *Rudarsko-Geološko-Naftni Zbornik*, *40*(5), 43–56. https://doi.org/10.17794/rgn.2025.5.4

Azis, B. N. L., Sariningtyas, G. C., Ardiansyah, W., Wulandari, S., & Muhammad Azis Albar. (2022). Identification of Geothermal Manifestation With Integration of Geomagnetic Data and Landsat-8 Satellite Imaging in Umbul Temple - Telomoyo, Central Java. *PIT IAGI 51st 2022* .

Bian, Y., Ni, Y., Guo, Y., Wen, J., Chen, J., Chen, L., & Yang, Y. (2024). Urban Geothermal Resource Potential Mapping Using Data-Driven Models—A Case Study of Zhuhai City. *Sustainability (Switzerland)*, *16*(17). https://doi.org/10.3390/su16177501

Blakely, R. J. (1995). *Potential Theory in Gravity and Magnetic Applications*. Cambridge University Press, Cambridge Core.

Boumehdi, M., Hahou, Y., Amrouch, K., Berkat, N. E., Carneiro, J., Correia, A., & Sadki, O. (2025). New assessment of geothermal resources in Morocco: Evaluation of the curie point depth method using magnetic data for geothermal gradient and heat flow estimation. *Scientific African*, *28*. https://doi.org/10.1016/j.sciaf.2025.e02726

Chan, H.-P., & Chan, Y.-C. (2023). Thermal pattern at kueishantao (KST) volcano of Taiwan from satellite-observed temperatures and its implication. *Environmental Research Communications*. https://doi.org/https://doi.org/10.1088/2515-7620/ace760

Chen, W., Tenzer, R., Xu, X., Wang, S., & Wang, B. (2021). Moho Depth Estimation Beneath Tibet From Satellite Gravity Data Based on a Condensation Approach. *Earth and Space Science*, *8*(6).

Demarco, N., Prezzi, C., & Bettucci, S. (2021). Review of Curie point depth determination through different spectral methods applied to magnetic data. *Geophysical Journal International*, *224*(1), 17–39. https://doi.org/10.1093/gji/ggaa361/5881306

Ejiga, E. G., Yusoff, I. Bin, el Hidayah, N., & Kumar, R. (2022). Geothermal energy assessment through the Curie point depth, geothermal gradient, and heat flow around the Akiri hot spring region in Central Nigeria. *Environmental Earth Sciences*, *81*(4).

Grant, M. A., & Bixley, P. F. (2011). *Geothermal reservoir engineering* (2nd ed.). Academic Press.

Hirt, C., Claessens, S., Fecher, T., Kuhn, M., Pail, R., & Rexer, M. (2013). New ultrahigh-resolution picture of Earth's gravity field. *Geophysical Research Letters*, *40*(16), 4279–4283. https://doi.org/10.1002/grl.50838

Hutauruk, S. A. Y., Sabrian, P. G., Putri, R. I., Saepuloh, A., & Shoedarto, R. M. (2024). Identification of geothermal pathways by fault fracture density (ffd) and gravity methods in Karangan sub-district, East Kutai district, East Kalimantan province. *IOP Conference Series: Earth and Environmental Science*, *1373*(1). https://doi.org/10.1088/1755-1315/1373/1/012031

Indriana, R. D. (2019). Distribution of subsurface anomalies in the Muria Peninsula and depth analysis with euler deconvolution. *International Journal of Physical Sciences and Engineering*, *3*(3), 21–30. https://doi.org/10.29332/ijpse.v3n3.355

Kassa, M., Alemu, A., & Muluneh, A. (2022). Determination of Conrad and Curie point depth relationship with the variations in lithospheric structure, geothermal gradient and heat flow beneath the central main Ethiopian rift. *Heliyon*, *8*(11). https://doi.org/10.1016/j.heliyon.2022.e11735

Kongpet, P., & Kanjanapayont, P. (2024). Curie point depth from airborne magnetic data analysis for geothermal exploration in southern Thailand. *Journal of Asian Earth Sciences*, *261*. https://doi.org/10.1016/j.jseaes.2023.105984

Li, C. F., Lu, Y., & Wang, J. (2017). A global reference model of Curie-point depths based on EMAG2. *Scientific Reports*, *7*. https://doi.org/10.1038/srep45129

Li, Y., & Oldenburg, D. W. (1996). 3-D inversion of magnetic data. *Geophysics*, *61*(2), 394–408. https://doi.org/10.1190/1.1443968

Maden, N., Gelisli, K., Eyuboglu, Y., & Bektas, O. (2009). Determination of tectonic and crustal structure of the eastern pontide orogenic belt (NE Turkey) using gravity and magnetic data. *Pure and Applied Geophysics*, *166*(12), 1987–2006. https://doi.org/10.1007/s00024-009-0529-7

Meyer, B., Chulliat, A., & Saltus, R. (2017). Derivation and Error Analysis of the Earth Magnetic Anomaly Grid at 2 arc min Resolution Version 3 (EMAG2v3). *Geochemistry, Geophysics, Geosystems*, *18*(12), 4522–4537. https://doi.org/10.1002/2017GC007280

Mono, J. A., Ndougsa-Mbarga, T., Tarek, Y., Ngoh, J. D., & Owono Amougou, O. U. I. (2018). Estimation of Curie-point depths, geothermal gradients and near-surface heat flow from spectral analysis of aeromagnetic data in the Loum – Minta area (Centre-East Cameroon). *Egyptian Journal of Petroleum*, *27*(4), 1291–1299. https://doi.org/10.1016/j.ejpe.2018.07.002

Muckharom, A. A., Setyawan, A., Rahmani, I. Q., Dwi Indriana, R., & Martha, A. A. (2026). Geothermal Resource Assessment On Sumatra Island: Estimating Thermal Gradient And Heat Flow Based On Aeromagnetic Data Via Curie Point Analysis. *Journal of Applied Science and Engineering*, *31*, 26031017. https://doi.org/10.6180/jase.202608_31.017

Muhajir, M. A., Seminar, K. B., & Nelwan, L. O. (2023). Detecting thermal anomalies in lahendong geothermal prospect using ASTER TIR and Landsat 8. *Jurnal Pengelolaan Sumberdaya Alam Dan Lingkungan*, *13*(3), 494–503. https://doi.org/10.29244/jpsl.13.3.494-503

Okubo, Y., & Matsunaga, T. (1994). Curie point depth in northeast Japan and its correlation with regional thermal structure and seismicity. *Journal of Geophysical Research*, *99*(B11). https://doi.org/10.1029/94jb01336

Pramudya, A. N., Indriana], R. D., M Sabri, L. O., & Pahlevi, A. M. (2025). Gravity Data Decomposition through Upward Continuation and Wavelet Transform, Case Study at Muria Peninsula, Java Island, Indonesia. *International Journal of Research and Review*, *12*(3), 128–136. https://doi.org/10.52403/ijrr.20250318

Pratiwi, R. N. J., Martha, A. A., Hartono, H., Wijayanti, R., Muckharom, A. A., Kinanti, A. S. A., & Ngaeni, N. P. N. (2026). Identification of Subsurface Geological Structures of the Arjuno-Welirang Geothermal Potential Area Using the Gravity Method. *Malaysian Journal of Fundamental and Applied Sciences*, *22*(1), 90–101. https://doi.org/10.11113/mjfas.v22n1.4573

Prihatini, A., Indriana, R. D., Setyawan, A., & Fahmi, M. (2025). Seismotectonic Characteristics of the Cugenang Fault, Cianjur, West Java, Based on a-Value, b-Value, Seismic Moment and Satellite Gravity (Earthquake Data of 2008-2023). *Sains Malaysiana*, *54*(8), 1889–1900. https://doi.org/10.17576/jsm-2025-5408-02

Putri, D. R., Ismail, N., Idroes, R., Rizal, S., Nur, S., & Nanda, M. (2021). Analysis of Land Surface Temperature (LST) in Bur Ni Geureudong Geothermal Field, Aceh, Indonesia Using Landsat 8 OLI / TIRS Images. *Chiang Mai University Journal of Natural Sciences*, *20*(4), 1–13. https://doi.org/10.12982/CMUJNS.2021.084

Rabuffi, F., Musacchio, M., Silvestri, M., Cianfarra, P., Salvini, F., & Buongiorno, M. F. (2025). Integrating satellite remote sensing and proximal data to investigate the role of brittle tectonics in the distribution of geothermal surface manifestations. Insights from the Parco Naturalistico delle Biancane - Larderello geothermal field (Southern Tuscany, Italy). *Geothermics*, *132*. https://doi.org/10.1016/j.geothermics.2025.103428

Rafiq, J., Abu-Mahfouz, I. S., Chavanidis, K., Arrofi, D., & Soupios, P. (2025). Spatial distribution of structural lineaments in the Al-Lith geothermal field, western Saudi Arabia: Remote sensing and aeromagnetic data analysis. *Journal of Asian Earth Sciences: X*, *13*. https://doi.org/10.1016/j.jaesx.2025.100191

Saada, S. A. (2016). Curie point depth and heat flow from spectral analysis of aeromagnetic data over the northern part of Western Desert, Egypt. *Journal of Applied Geophysics*, *134*, 100–111. https://doi.org/10.1016/j.jappgeo.2016.09.003

Saraswati, G. P., Prasetyo, Y., & Sukmono, A. (2019). Analisis Estimasi Energi Panas Bumi Dan Rekomendasi Lokasi Pembangkit Listrik Tenaga Panas Bumi Menggunakan Citra Landsat 8 (Studi Kasus : Kawasan Gunung Ungaran, Jawa Tengah). *Jurnal Geodesi Undip Januari*, *8*(1), 170–179. https://doi.org/https://doi.org/10.14710/jgundip.2019.22554

Setyawan, A., Khusna, L. M., Suseno, J. E., Rina, D. I., Yulianto, T., & Aribowo, Y. (2021). Detecting hot spring manifestations based on gravity data satellite on mountain Lawu. *Journal of Physics: Conference Series*, *1943*(1). https://doi.org/10.1088/1742-6596/1943/1/012034

Setyawan, A., Nadhila, M. F., Suseno, J. E., & Indriana, R. D. (2024). 2d Sparse Inversion Gravity Method For Subsurface Interpretation By Simpeg: A Case Study Of Ungaran Volcano. *Journal of Southwest Jiaotong University*, *59*(3). https://doi.org/10.35741/issn.0258-2724.59.3.36

Setyawan, A., Yudianto, H., Nishijima, J., & Hakim, S. (2015). Horizontal Gradient Analysis for Gravity and Magnetic Data Beneath Gedongsongo Geothermal Manifestations, Ungaran, Indonesia. *Proceedings World Geothermal Congress*, 19–25.

Telford, W., Geldart, L., & Sheriff, R. (1990). *Geofisika Terapan* (2nd ed.). Cambridge University Press.

Weldeyohannes, T. T., Hailu, B. T., Muluneh, A. A., & Kidane, T. (2022). Detection of geothermal anomalies in the Northern Lake Abaya geothermal field, Main Ethiopian Rift. *Journal of Volcanology and Geothermal Research*, *430*. https://doi.org/10.1016/j.jvolgeores.2022.107638